International Journal of Applied Earth Observation and Geoinformation 143 (2025) 104770

Contents lists available at ScienceDirect

International Journal of Applied Earth Observation and Geoinformation

journal homepage: www.elsevier.com/locate/jag

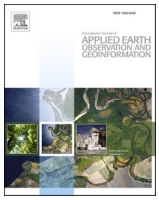

# Rheological and tectonic implications of eastern Tibet: Insights from early aftershock sequences driven by afterslip following three 2021–2022 moderate-large events

Xiaoge Liu [a,b,c], Wenbin Xu [b,*], William B. Frank [d], Yijian Zhou [e], Guoqiang Zhao [b,f], Lihua Fang [f], Hui Huang [g], Lijia He [h], Weijun Gan [i]

[a] State Key Laboratory of Geohazard Prevention and Geoenvironment Protection, College of Earth and Planetary Sciences, Chengdu University of Technology, Chengdu 610059, China
[b] Laboratory of Volcano and Earthquake Research, School of Geosciences and Info-Physics, Central South University, Changsha 410083 Hunan, China
[c] Now at Physical Science and Engineering Division, King Abdullah University of Science and Technology (KAUST), Thuwal 23955-6900, Saudi Arabia
[d] Department of Earth, Atmospheric and Planetary Sciences, Massachusetts Institute of Technology, Cambridge, MA, USA
[e] Division of Geological and Planetary Sciences, California Institute of Technology, Pasadena, CA, USA
[f] Institute of Earthquake Forecasting, China Earthquake Administration, Beijing 100036, China
[g] State Key Laboratory of Marine Geology, Tongji University, Shanghai 200092, China
[h] Earth Observatory of Singapore, Nanyang Technological University, Singapore
[i] State Key Laboratory of Earthquake Dynamics, Institute of Geology, China Earthquake Administration, Beijing 100029, China

ARTICLE INFO

*Keywords:*
Early aftershock and afterslip
Complementary aftershock and coseismic slip and afterslip
Transient brittle-ductile transition depth
Fault frictional heterogeneity
Rheological and tectonic implications

ABSTRACT

Early aftershock sequences and afterslip provide key insights into crust rheology and the triggering mechanisms of seismicity sequences. Three recent moderate-large strike-slip earthquakes in eastern Tibet, including the 2021 Yangbi Mw 6.1, the 2021 Maduo Mw 7.4, and the 2022 Menyuan Mw 6.4 events, provide an ideal opportunity to investigate the driving processes of aftershocks and the regional crustal rheology. In this study, we inverted for the early afterslip and statistically analyzed the spatiotemporal evolution of these three aftershock sequences. Our results reveal a significant spatial complementarity between the relocated aftershocks, coseismic slip and early afterslip, suggesting aftershocks were triggered by afterslip driven by the coseismic stress changes. The depth of the aftershock sequences consistently shallows over time, which we interpret as a transient response of the brittle-ductile transition zone to early postseismic relaxation. For the first time, we quantify the depth-dependent variations of aftershock-derived rheological and frictional parameters along these three strike-slip faults in eastern Tibet. The recurrence times derived from early aftershocks are generally shorter than those estimated from geodetic or geological data, demonstrating that fault loading rates are not constant throughout the seismic cycle. This spatiotemporal comparison between aftershocks, coseismic slip and afterslip allows for the discrimination of different aftershock driving mechanisms. The framework presented here is generalized to other similar tectonic settings, providing a method to identify the dominant aftershock driving mechanism and to constrain the rheological properties, frictional parameters and recurrence times of regular earthquakes.

## 1. Introduction

Early aftershock sequences provide important information about the brittle-ductile transition, rheological and frictional properties of the seismogenic fault interface (Cheng and Ben-Zion, 2019; Frank et al., 2017; Perfettini et al., 2019; Rolandone et al., 2004), which are crucial for understanding regional seismotectonics and earthquake hazards. Early aftershocks are also essential for understanding the mechanisms of seismic triggering processes, including pore fluid diffusion (Chen et al., 2012; Dublanchet and De Barros, 2021; Duverger et al., 2015), the coseismic stress disturbance, aseismic afterslip and/or viscous flow (Frank et al., 2017; Liu and Xu, 2019; Peng and Zhao, 2009; Perfettini et al., 2010; Perfettini et al., 2019).

Since May 2021, three moderate-to-large strike-slip earthquakes

* Corresponding author.
*E-mail address:* wenbin.xu@csu.edu.cn (W. Xu).

https://doi.org/10.1016/j.jag.2025.104770
Received 14 April 2025; Received in revised form 29 July 2025; Accepted 29 July 2025
Available online 5 August 2025

occurred in eastern Tibet (Fig. 1). On 21 May 2021, the dextral strike-slip Yangbi Mw 6.1 earthquake occurred in southeast Tibet as a typical foreshock-mainshock-aftershock sequence (Liu et al., 2022c; Wang et al., 2024; Zhang et al., 2021b). One day later, the sinistral strike-slip Maduo Mw 7.4 earthquake occurred within the Bayan Har Block, which is the largest event in China since the 2008 Mw 7.9 Wenchuan earthquake (Li et al., 2025; Su et al., 2022; Wen et al., 2024; Zhao et al., 2021; Zhao et al., 2022). On 8 January 2022, the sinistral strike-slip Menyuan Mw 6.7 earthquake ruptured the western Lenglongling Fault belonging to the Qilian-Haiyuan sinistral fault system (He et al., 2024; Liu et al., 2022a; Yang et al., 2022; Yu et al., 2024). However, the dominant triggering processes of seismicity sequences following these three events are either still subject to debate or not well constrained. For instance, diverse mechanisms are proposed to explain the foreshock sequence of the Yangbi earthquake (e.g. cascade triggering (Zhang et al., 2021b), fluid flow (Lei et al., 2021) or both aseismic slip and cascade triggering (Liu et al., 2022c). In comparison, the Yangbi aftershock sequence was triggered by both postseismic relaxation and coseismic stress (Liu et al., 2022c). The coseismic stress triggering (Feng et al., 2022) and possible afterslip (Fan et al., 2022) are proposed to explain the aftershock sequence following the 2022 Menyuan mainshock. Similarly, following the 2021 Maduo mainshock, the coseismic stress loading (Zhao et al., 2022) and afterslip (He et al., 2021) are proposed to address the aftershock sequence. It is still unclear which mechanism is dominating the dynamics of these aftershock sequences. Thus, further study of the dominant aftershock triggering mechanisms is important to understand regional seismic hazards. In addition, the three earthquakes are located in different regions from south to north along the East Tibet (Fig. 1), with different tectonic backgrounds (e.g., different heat flow (Hu et al., 2000) and diverse velocity structures (Shen et al., 2016)). It is thus worth investigating whether there are commonalities or unique characteristics for these three earthquakes reflected in the aftershock sequences.

In this study, we use Interferometric Synthetic Aperture Radar (InSAR) data to map the early afterslip and investigate the spatiotemporal distributions of the early seismicity sequences following the 2021 Yangbi Mw 6.1, the 2021 Maduo Mw 7.4 and the 2022 Menyuan Mw 6.7 earthquakes. We compare the aftershock sequences, coseismic slip and afterslip models and analyze the moment release ratio of aftershocks to afterslip, which is important to discriminate different aftershock driving mechanisms. We also analyze the rapid temporal shallowing of the brittle-ductile transition depth associated with the rapid postseismic relaxation revealed by the early aftershock sequences. Finally, we estimate the rheological and frictional parameters and the recurrence times of earthquakes in comparison to geodetically or geologically derived parameters. The results shed light on the important role of early aseismic slip in the spatiotemporal characteristics of early aftershock expansion and suggest that early aftershock sequences could provide alternative constraints on the deep-earth rheology and recurrence time estimates.

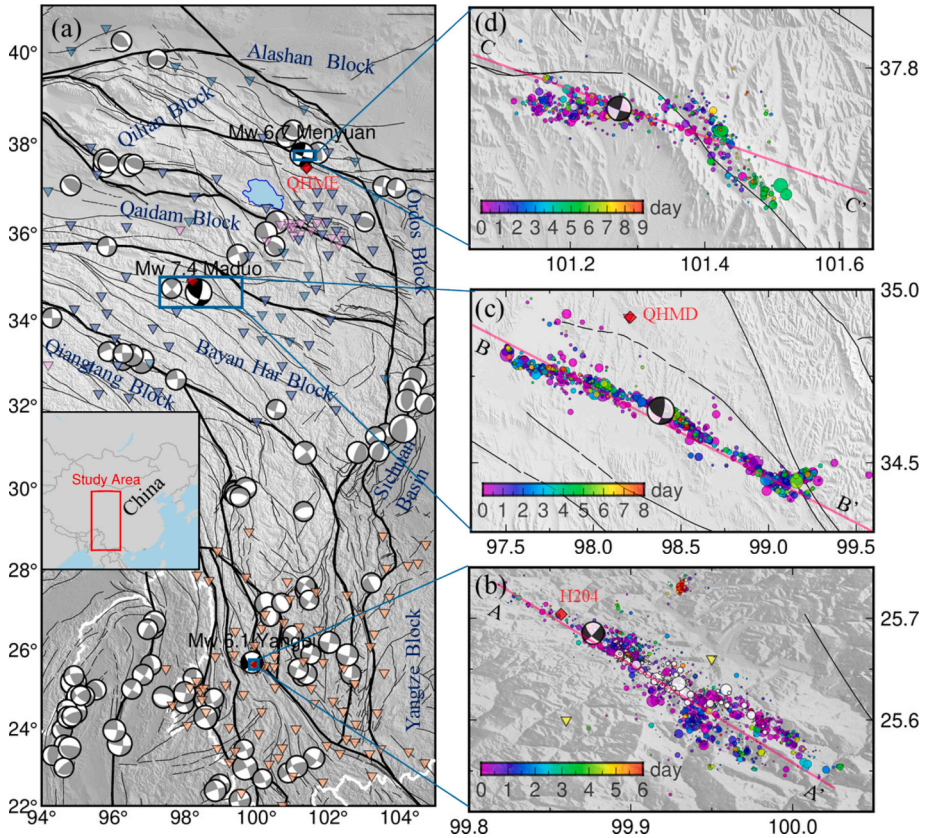


**Fig. 1.** Regional seismotectonic context around the 2021 Yangbi Mw 6.1, the 2021 Maduo Mw 7.4 and the 2022 Menyuan Mw 6.7 earthquakes. (a) Black focal mechanisms represent the relocated epicenters of the three strike-slip mainshocks. Gray focal mechanisms represent historical events with Mw > 5.5 from Global Centroid Moment Tensor (GCMT, https://www.globalcmt.org/). Brown, purple and blue triangles are seismic stations used for relocation of the Yangbi, the Maduo and the Menyuan sequences (Fan et al., 2022; Wang et al., 2021; Yang et al., 2021). Seismic stations in the Maduo and the Menyuan cases are partially overlapped. Red diamonds are GNSS stations. Thick black lines are the main block boundary faults and thin black lines are active faults. (b), (c) and (d) are the detailed relocated sequence with color-coded times for the Yangbi, the Maduo and the Menyuan cases, respectively. The purple lines are the profiles A-A', B-B' and C-C' used in the following analysis. The white dots in (b) are the Yangbi foreshock sequence. (For interpretation of the references to color in this figure legend, the reader is referred to the web version of this article.)

## 2. Early postseismic deformation and afterslip models

One Sentinel-1 interferogram for the Maduo, and one for the Menyuan are used to retrieve the early postseismic line-of-sight (LOS) displacements following the 2021 Maduo and 2022 Menyuan earthquakes (Table S1). Based on the standard two-pass InSAR data processing procedures (Xu et al., 2016), the corresponding postseismic displacement fields were generated using GAMMA software (Fig. 2). For the Maduo case, the descending interferogram well captured the early postseismic displacement with a maximum of ~ 3 cm surface displacement towards the satellite in the radar line of sight (LOS), while the ascending interferogram shows a relatively noisier result with smaller LOS displacements (Fig. 2). Deformation characteristics of opposite polarities on both sides of the seismogenic fault in both ascending and descending tracks indicate that sinistral slip dominated the postseismic deformation after the Maduo mainshock. Only the descending interferogram is available for the Menyuan early postseismic displacement, which shows that the main postseismic displacement of up to ~ 1 cm occurred southeast of the mainshock. We also processed the postseismic Yangbi interferogram but no observable postseismic slip was present due to poor signal-to-noise ratio and the smaller moment magnitude of the Yangbi earthquake.

Following a two-step geodetic inversion strategy similar to Xu (2017), we first constrained the fault geometry and then solved for the slip distribution. In the first step, a nonlinear, Monte Carlo-type simulated annealing algorithm was used to find the optimal single-plane fault geometry assuming uniform slip. In the second step, this fault geometry was fixed, enlarged, and discretized into smaller patches, after which a

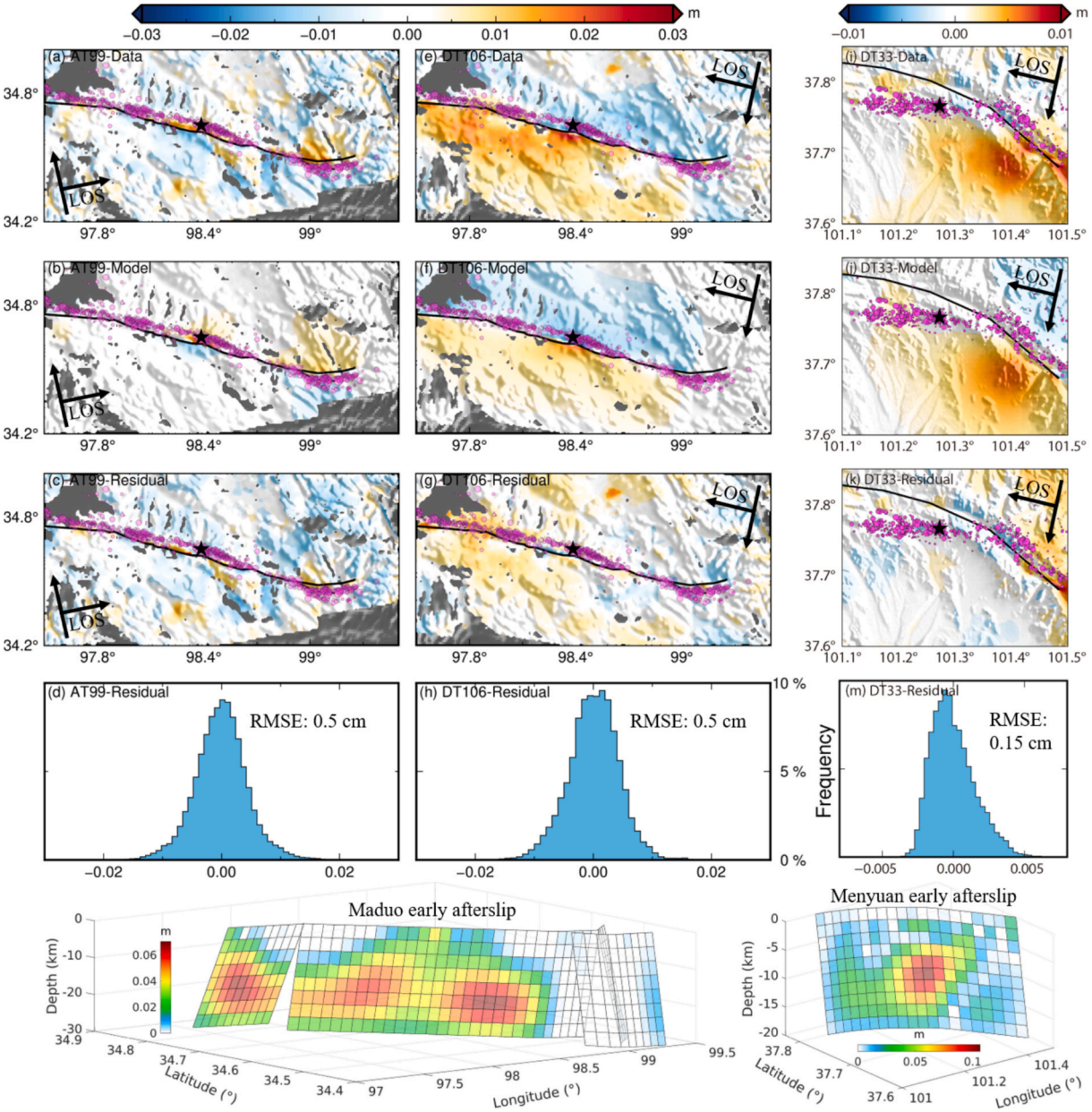


**Fig. 2.** Observed and modeled early postseismic ground displacement in satellite line of sight (LOS) for both (a-d) ascending and (e-h) descending tracks for the 2021 Maduo earthquake, and (i-m) descending track for the 2022 Menyuan earthquake. Warm colors indicate LOS displacement towards the satellite. First row: the observed ground deformation fields; Second row: model predictions; Third row: residuals between observations and models; Fourth row: histogram of residuals. Bottom row shows the preferred Maduo and the Menyuan early afterslip models. Black lines and stars represent the surface trace of the modeled seismogenic fault and the relocated epicenter, respectively. Purple dots represent aftershocks (M > Mc, see the following text). Note the different color scales for the Maduo case and Menyuan case. (For interpretation of the references to color in this figure legend, the reader is referred to the web version of this article.)

linear least-squares inversion with Laplacian smoothing was applied to determine the variable slip on each patch. Distributed early afterslip is linearly inverted from early postseismic observations (Fig. 2). The inverted afterslip models of the Maduo (12–26 km depth) and Menyuan (8–14 km depth) cases indicate postseismic fault deformation occurred downdip of the coseismic ruptures (Fig. 2). The predicted displacements from the preferred afterslip models explain both ascending and descending postseismic observations well, with a root-mean-square error (RMSE) of ~ 0.5 cm from residuals for the Maduo case (Fig. 2d) and 0.15 cm for the Menyuan case (Fig. 2m). Assuming the shear modulus of 30 GPa, we calculated the geodetic moment ($M_0$) as ~ 1.06 × $10^{18}$ Nm and 5.7 × $10^{17}$ Nm from the afterslip models, which are equivalent to $M_w$ 5.95 and $M_w$ 5.7 for the Maduo earthquake and Menyuan earthquake, respectively (Table S2).

## 3. Spatiotemporal evolutions of seismicity relocation catalogs

We use three recently published relocated seismicity catalogs, which were generated with the same state-of-the-art methodology: the double-difference (hypoDD) relative relocation algorithm (Waldhauser and Ellsworth, 2000) to ensure the location accuracy needed for fine-scale spatiotemporal analysis. For the 2021 Yangbi Mw 6.1 earthquake, we adopted the catalog from Yang et al. (2021), which reports the mean EW, NS and vertical location errors of approximately 0.19 km, 0.20 km and 0.27 km, respectively. For the 2021 Maduo Mw 7.4 event, we utilized the catalog from Wang et al. (2021), with reported uncertainties of approximately 0.24 km (EW), 0.27 km (NS) and 0.5 km (vertical). The catalog for the 2022 Menyuan earthquake is from Fan et al. (2022), with associated errors of about 0.38 km (EW), 0.35 km (NS) and 0.57 km (vertical). These catalogs have been used widely in recent published works (Li et al., 2022; Liu et al., 2022c; Su et al., 2022; Zhao et al., 2021). Based on these relocated catalogs, we estimated the corresponding overall magnitude of completeness (Mc) and b-value using the maximum likelihood method, as implemented in the ZMAP software package (Wiemer, 2001). We find an overall Mc of 0.1, 0.7 and 0.6, and b-values of 0.59, 0.55 and 0.63, respectively, for the 2021 Mw 6.1 Yangbi earthquake, the 2021 Mw 7.4 Maduo earthquake and the 2022 Mw 6.7 Menyuan earthquake (Fig. S1). A total of 1368 (Yangbi), 981 (Maduo) and 565 (Menyuan) events above the corresponding Mc values are used in the following analysis.

While the 2021 Yangbi sequence exhibited foreshocks, the two other cases are mainshock-aftershock sequences. All three earthquake sequences are distributed in a similar NW–SE orientation but with specific strike directions and different segmentations (Fig. 3a and Fig. S2). The Yangbi foreshocks have been suggested to trigger the mainshock (Liu et al., 2022c; Zhu et al., 2022). The largest Ms 5.2 aftershock of the Yangbi case occurred ~ 40 min after the mainshock at the southeastern end of the aftershock zone (Fig. 3a). The aftershocks following the Maduo mainshock occurred on both sides of the mainshock indicating a bilateral coseismic rupture (Fig. 3b and Fig. S3). The largest Ms 5.2 aftershock occurred ~ 8 h after the 2021 Maduo mainshock at the northwest tip of the aftershock sequence. Similar to the Maduo case, the aftershock distribution following the Menyuan earthquake also indicates a bilateral rupture characteristic, which is consistent with the joint coseismic rupture inversion of geodetic and seismological data (He et al., 2024). At the southeastern end of the Menyuan aftershock zone (Fig. 3c and Fig. S4), the largest dextral strike-slip Ms 5.3 aftershock occurred ~ 4 days after the sinistral mainshock (He et al., 2024) and caused observable surface deformation, which was removed prior to our afterslip model inversion.

Both the Maduo and Menyuan mainshocks occurred at the locations with marked strike variations, so-called fault linkage point, which are conducive to stress accumulation and eventually become the nucleation sites (Fig. 3). One common feature in the depth-distance distributions for these three cases is the presence of multiple seismic clusters (third column in Fig. 3). The Yangbi and Menyuan cases both have two clusters, while Maduo has at least four clusters, which may reflect the heterogeneous characteristics of the faults (Soto et al., 2019; Yoshida et al., 2020). In addition, we observed several seismic gaps (e.g., G1-G5 in Fig. 3) and seismicity clusters (e.g., C1-C8 in Fig. 3) in the aftershock sequences, which we discuss in Section 4.1. Interestingly, the temporal depth evolution of the three earthquake sequences is all characterized by relatively deep events occurring close to the mainshock onsets, followed by a migration to shallower depths (Fig. 3 and Fig. S2-4), which will be statistically analyzed in Section 4.2. Moreover, rheological and tectonic implications derived from these aftershock sequences will be discussed in Section 4.3.

## 4. Discussions

### 4.1. Relation between aftershock Sequences, coseismic slip and afterslip

The aftershock sequences following the three recent strong earthquakes in eastern Tibet are characterized by logarithmic cumulative event counts (Fig. 4 and Fig. S5). All three aftershock sequences migrate in the along-strike direction with different average migration speeds estimated by the migration distance divided by the corresponding time interval (Fig. 4). For the Yangbi and Menyuan sequences, the speeds of SE migration (~5 km/day) are both higher than those of NW propagation (~1 km/day), which could potentially be attributed to the differences in coseismic slip to the NW and SE (i.e., dominant SE coseismic slip) (Fig. 5). The migrations of Maduo aftershocks have much larger speeds of ~ 100 km/day, which can be explained by the migration velocity that should scale with the size of the earthquake, as predicted by an analytical model (Perfettini et al., 2019). However, the similar migration velocities in both the Yangbi and Menyuan cases, despite their different magnitude, indicate that other regional tectonic differences (e.g., possible rheological contrast) should be considered to explain the migration velocity differences. These spatiotemporal migrations and the logarithmic increase in aftershock counts are generally thought to be driven by afterslip (Frank et al., 2017; Liu et al., 2022c; Peng and Zhao, 2009). Moreover, the largest aftershocks of the three cases all occurred at the aftershock migration fronts (Fig. 4). These observations suggest that afterslip likely plays an important role in triggering aftershocks. Eight aftershock clusters (C1-C8 in Fig. 3) are identified in the three aftershock sequences, which may be related to structural features (Soto et al., 2019; Yoshida et al., 2020). One seismic gap G1 between the clusters C1 and C2 is well filled by the 2021 Yangbi foreshocks (Fig. 1b, 4 and 5). This implies that the Yangbi foreshocks have substantially released accumulated stress in the gap G1. This complementary pattern of foreshocks and aftershocks is also observed in other sequence (Yoshida et al., 2020). In the Menyuan case, two seismicity clusters C7 and C8 separated by the gap G5 can be well explained by the early afterslip model (Fig. 5), which indicates the gap G5 is characterized by significant velocity-strengthening frictional behavior inhibiting earthquake nucleation (Liu and Xu, 2019; Perfettini et al., 2019). Four clusters C3-C6 and three gaps G2-G4 are identified in the Maduo case (Figs. 4 and 5), indicating more complex fault ruptures and regional crustal heterogeneity than in the other two sequences (Soto et al., 2019; Yoshida et al., 2020). The gaps G2 and G4 are attributed to the relatively complete coseismic rupture of asperities during the Maduo mainshock, while the gap G3 can be explained by the estimated early postseismic slip (Fig. 5). Compared with one main asperity rupture in the Yangbi and Menyuan cases (Fig. 5a and c), the Maduo mainshock ruptured at least five asperities mainly at shallow depth (< 10 km), which are spatially complementary to but partially overlap with the relatively deep (5–15 km) aftershocks (Fig. 5c). Similarly, this complementary pattern of shallow mainshock ruptures and deep aftershocks is also observed in both the Yangbi and Menyuan cases. This supports that coseismic stress disturbances play a crucial role in the generation of aftershocks.

The afterslip distributions observed in both the Maduo and Menyuan cases are also complementary to both aftershocks and coseismic rup-

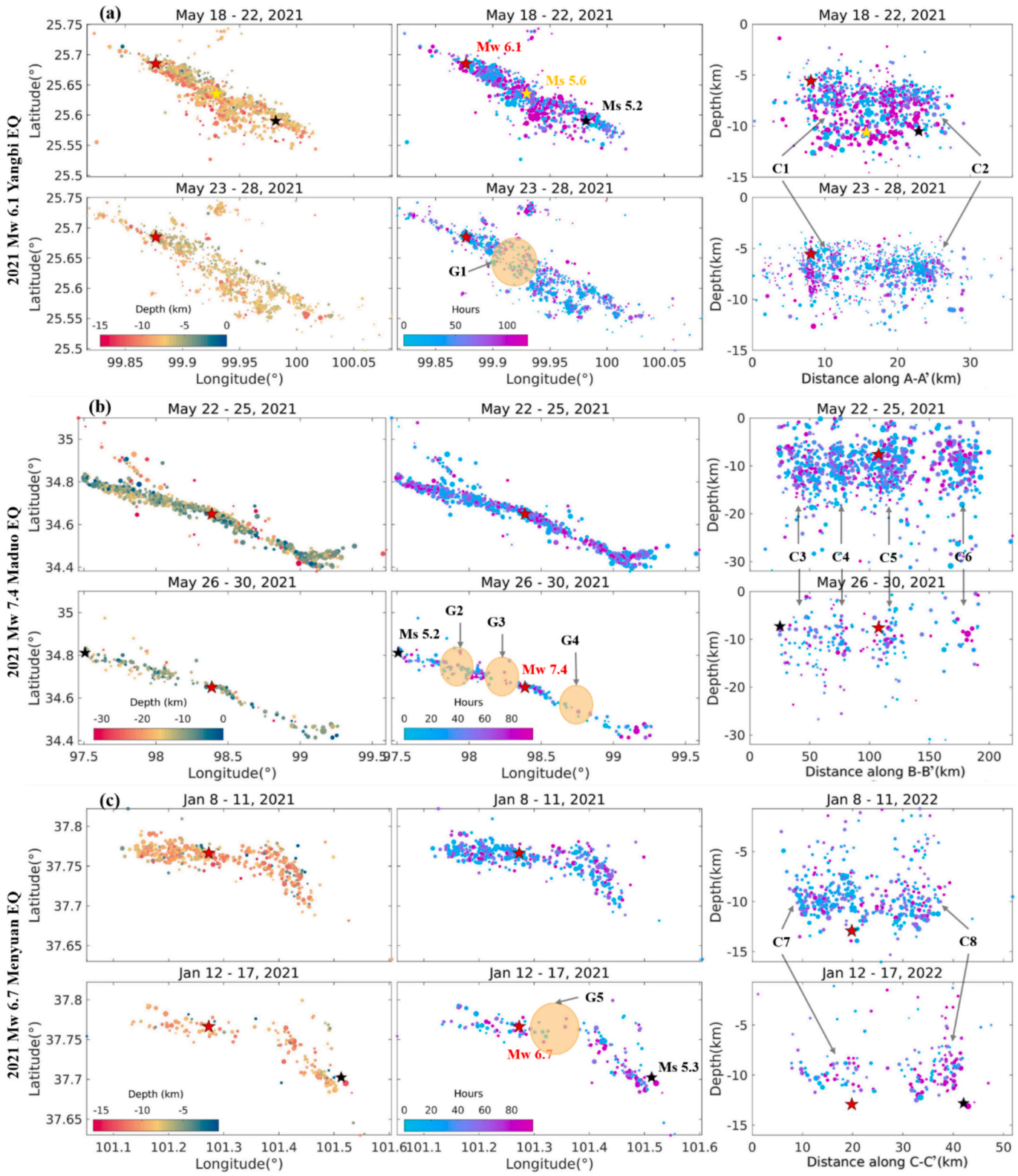


**Fig. 3.** Spatiotemporal distributions of seismicity sequences for (a) the 2021 Mw 6.1 Yangbi earthquake, (b) the 2021 Mw7.4 Maduo earthquake and (c) the 2022 Mw 6.7 Menyuan earthquake. First column: Spatiotemporal distributions with color-coded depth; Second column: Spatiotemporal distributions with color-coded time; Third column: Seismicity plots of distance along profiles (Fig. 1) versus depth with color-coded time. Red and black stars represent the mainshocks and the largest aftershocks, respectively. The yellow star indicates the largest foreshock of the 2021 Mw 6.1 Yangbi earthquake. (For interpretation of the references to color in this figure legend, the reader is referred to the web version of this article.)

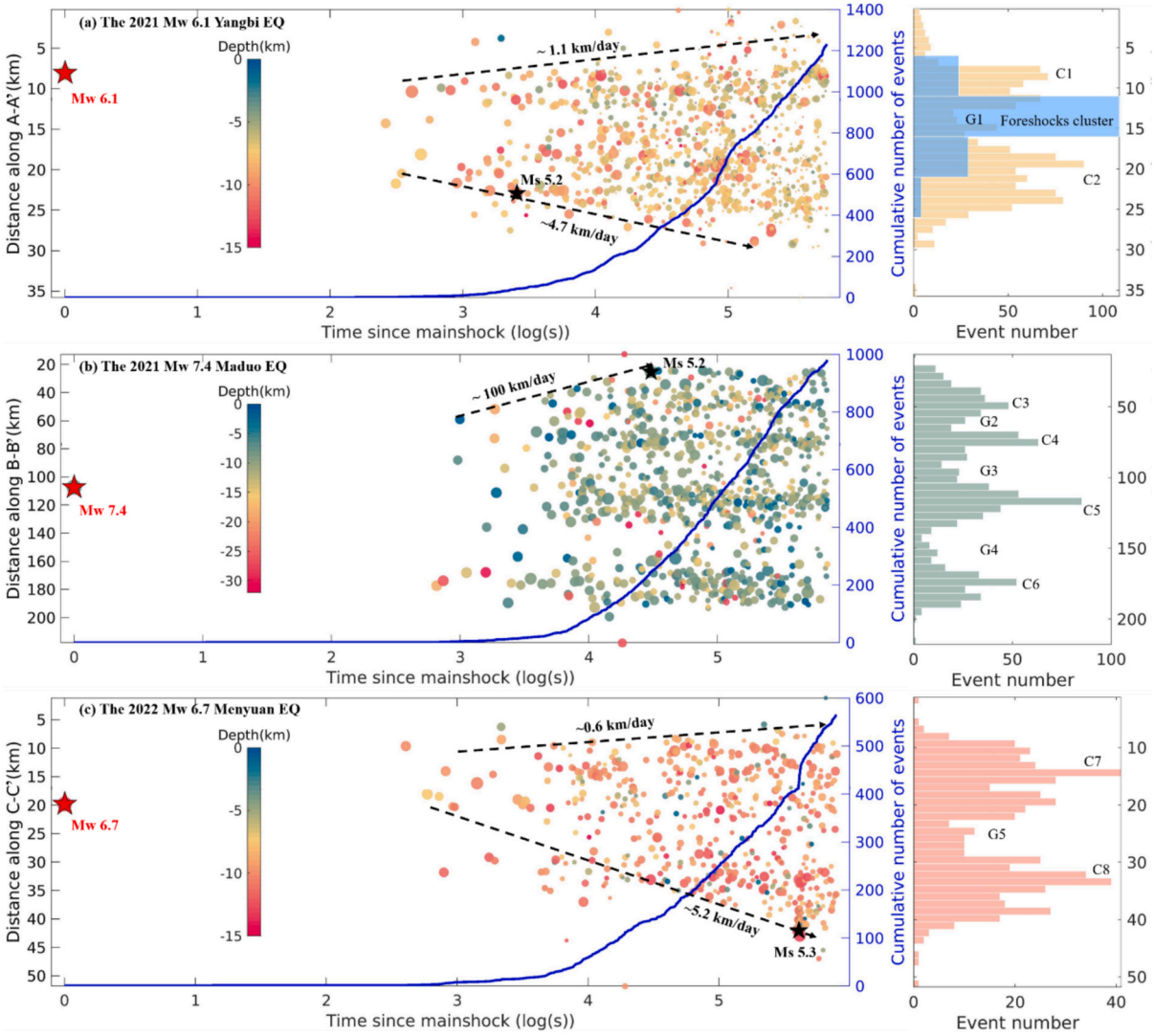


**Fig. 4.** Spatiotemporal evolution with logarithmic time of aftershocks along profiles (Fig. 1) for (a) the 2021 Mw 6.1 Yangbi earthquake, (b) the 2021 Mw7.4 Maduo earthquake and (c) the 2022 Mw 6.7 Menyuan earthquake. Aftershocks are colored by depth and scaled by magnitude. The mainshocks and the largest aftershocks for different cases are plotted as red and black stars, respectively. The blue line indicates the cumulative number of events. The black dashed lines with arrows mark the approximate aftershock migration fronts along the causative fault labeled with migration rates. The labeled migration speeds are the mean velocities. The right-side histograms show the event distance histogram along respective profiles. Eight aftershock clusters C1-C8 and five seismic gaps G1-G5 are clearly identified. The transparent blue bars in (a) are the Yangbi foreshocks (see also in Fig. 1b and Fig. 5a). (For interpretation of the references to color in this figure legend, the reader is referred to the web version of this article.)

tures (Fig. 5), which are also observed in other cases (Huang et al., 2017; Jiang et al., 2021), supporting the significant role of afterslip in the behavior of aftershock sequences. In addition, seismicity clusters/streaks surrounding creep zones are considered as markers of aseismic slip (Fig. 4), a process that loads numerous velocity-weakening patches hosting seismic events (Soto et al., 2019). Additionally, we found that the aseismic moment releases of $10.6 \times 10^{17}$ Nm (Mw 5.95) and $5.7 \times 10^{17}$ Nm (Mw 5.77) from the early afterslip for the Maduo and Menyuan cases, respectively (Table S2). However, the moment releases from aftershocks within the same periods are only $5.9 \times 10^{16}$ Nm (Mw 5.24) and $1.8 \times 10^{16}$ Nm (Mw 4.78), respectively, corresponding to about 6 % and 3 % of their respective afterslip moment releases. This indicates that aseismic slip is dominant during the postseismic moment release and plays a significant role in triggering aftershocks. Considering the directional seismicity migrations (Fig. 4), the complementary spatial pattern between aftershocks, coseismic slip and afterslip (Fig. 5), a similar logarithmic increase in accumulated afterslip amplitude and aftershocks number (Kato and Obara, 2014; Liu and Xu, 2019; Peng and Zhao, 2009; Perfettini et al., 2019), we suggest that coseismic stress loading drove subsequent aseismic slip, which governed the postseismic stress redistribution and triggered aftershocks on small asperities. This likely scenario is consistent with the analytical models of how aftershocks migrate along strike driven by mainshock and afterslip (Perfettini et al., 2018, 2019), and provides a reasonable explanation for why the largest Mw 5.2 aftershock occurred right near the aseismic slip zone with a ~ 8 h delay after the Maduo mainshock (Figs. 3 and 5).

Fluid diffusion at depth has also been suggested to explain the migrations of seismic sequences (Chen et al., 2012; Dublanchet and De Barros, 2021; Duverger et al., 2015). However, fluid-driven seismicity fronts migrate with square root of time (Shapiro et al., 1997) and the migration velocity is typically on the order of m/d (Chen et al., 2012; Dublanchet and De Barros, 2021; Duverger et al., 2015), which is significantly smaller than the logarithmic migration at the speeds (1–100 km/day) observed in this study (Fig. 4). The observed migration speeds are comparable to the propagation velocity of shallow aseismic transients, on the order of a kilometer per hour (Roland and McGuire,

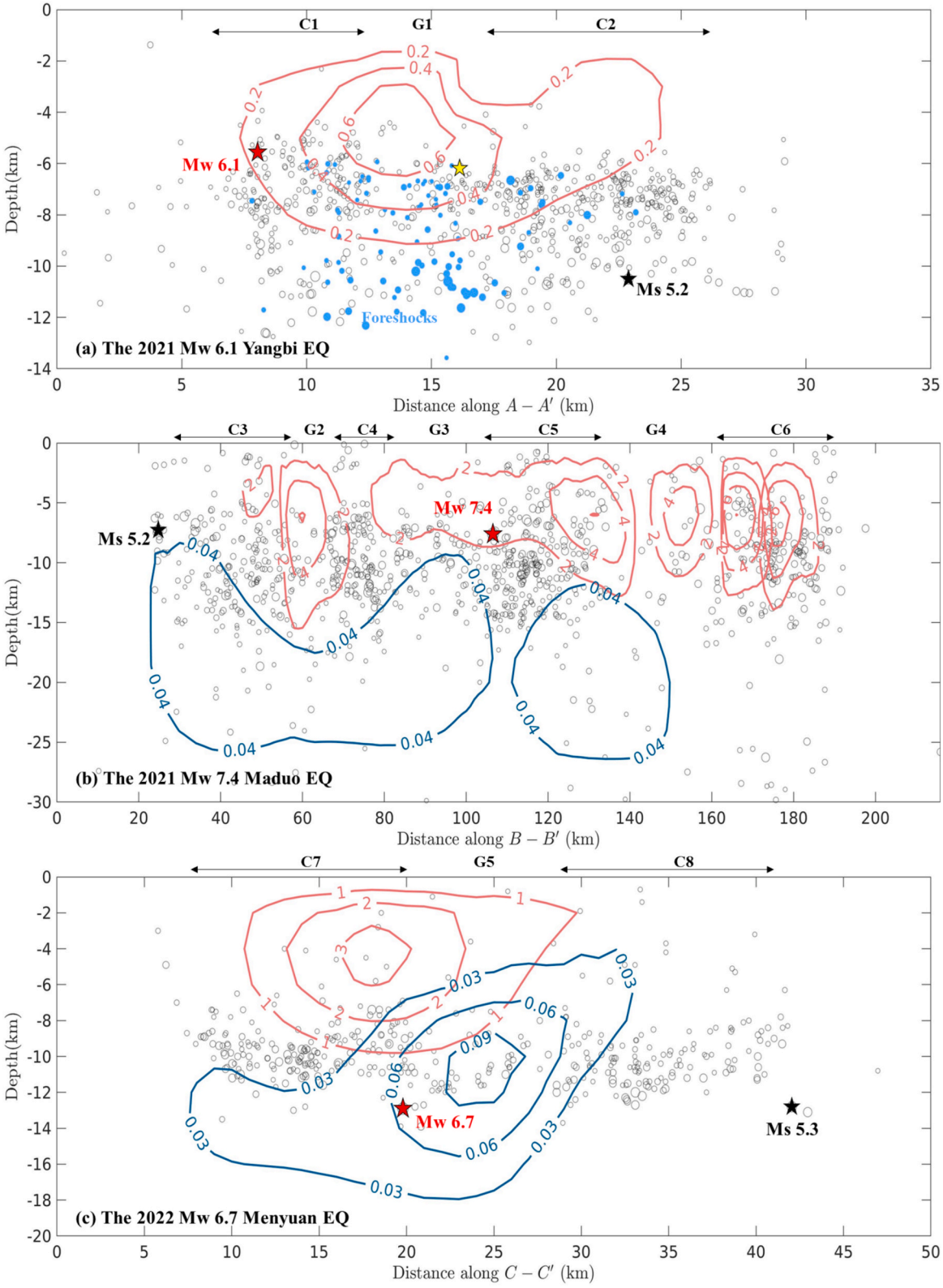


**Fig. 5.** Comparison between earthquake sequences, coseismic slip and/or afterslip for (a) the 2021 Mw 6.1 Yangbi earthquake, (b) the 2021 Mw7.4 Maduo earthquake and (c) the 2022 Mw 6.7 Menyuan earthquake. The smoothed red and blue contours labeled with different intervals in meters indicate the individual coseismic slip and afterslip, respectively. The gray circles represent the individual aftershocks and blue solid dots in (a) represent the Yangbi foreshocks. The mainshocks and the largest aftershocks for different cases are plotted as red and black stars, respectively. Eight seismicity clusters (C1-C8) and five seismic gaps (G1-G5) are identified. The Yangbi, Maduo and Menyuan coseismic slip models are adopted from (Li et al., 2022), (Zhao et al., 2021) and (He et al., 2024), respectively. (For interpretation of the references to color in this figure legend, the reader is referred to the web version of this article.)

2009). In addition, we also examined the distance versus time distribution of the shallow and deep aftershocks of the three cases, which show no obvious migration with square root of time (Fig. S5). We thus suggest that the characteristics of our observed aftershock sequences are best explained by the logarithmic afterslip model (Perfettini et al., 2018, 2019).

The generally complementary pattern observed between coseismic slip, afterslip, and their respective seismicity sequences illustrates that different segments of a fault release stress in different ways, indicating heterogeneous frictional properties (Yoshida et al., 2020). The spatial

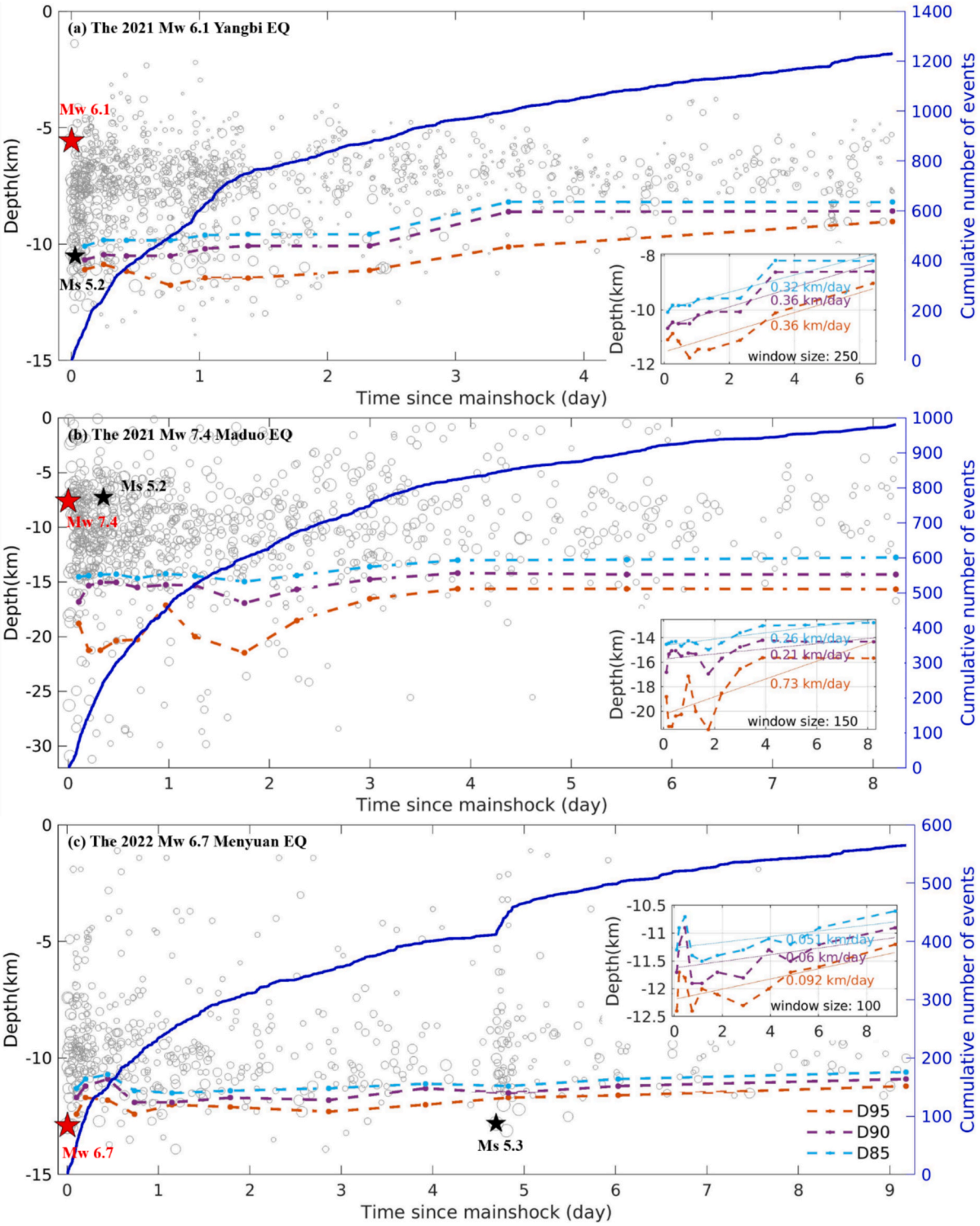


**Fig. 6.** Plots of depth versus time exhibiting the temporal evolution and transition depth variations of the aftershock sequences for (a) the 2021 Mw 6.1 Yangbi earthquake, (b) the 2021 Mw7.4 Maduo earthquake and (c) the 2022 Mw 6.7 Menyuan earthquake. Earthquakes are scaled by magnitude. The mainshocks and largest aftershocks are plotted as red and black stars, respectively. The blue line indicates the cumulative number of aftershocks. The colored dashed lines represent temporal variations of different transition depths (i.e., D85, D90, D95). The insets in each subplot show a zoomed-in view of the temporal transition depth. (For interpretation of the references to color in this figure legend, the reader is referred to the web version of this article.)

separation of coseismic slip and afterslip and seismicity sequences is pervasive in the different tectonic settings (Huang et al., 2017; Jiang et al., 2021; Liu and Xu, 2019), and it is well-established that such spatial separation is attributed to differences in the fault's frictional behavior (Jiang et al., 2021; Perfettini and Avouac, 2004). Specifically, fault patches with velocity-weakening (VW) properties are prone to unstable, seismic slip and thus host the coseismic rupture. In contrast, surrounding areas with velocity-strengthening (VS) properties favor stable, aseismic slip, which manifests as afterslip following the mainshock. In addition, seismicity clusters also suggest heterogeneous fault properties (Soto et al., 2019). Velocity-strengthening regions may contain small asperities on which aftershocks are triggered by coseismic stress-driven afterslip, which can explain the partial overlap of afterslip and aftershocks. In addition, the partial overlap between coseismic slip and afterslip may be due to neutral frictional behavior or a rate-dependent transition from rate-weakening at high sliding rates to rate-strengthening at lower rates (Perfettini and Avouac, 2014), and/or simply reflect the smoothing constraints employed in the fault slip inversion (Perfettini et al., 2010).

The interplay between seismic rupture on VW asperities and aseismic afterslip on surrounding VS areas, as observed in our study of eastern Tibet, is not a unique phenomenon. Our findings in Eastern Tibet are validated by comparisons with other active tectonic zones, such as Eastern Anatolia. While our study focuses on aftershocks driven by afterslip dominated by coseismic slip, the 2011 Mw 7.1 Van earthquake showed complex off-fault aftershocks on a "transfer fault" triggered by static stress changes (Toker et al., 2021). Both cases show that a major earthquake reorganizes crustal stress according to pre-existing heterogeneity. Another compelling parallel is the seismicity clustering in the Gulf of Gökova, Turkey, where Toker (2021) showed that distinct earthquake clusters on locked VW patches are driven by aseismic creep on surrounding VS segments. This is directly analogous to our model of afterslip-driven aftershocks, suggesting this mechanism is robust across diverse tectonic settings, from continental strike-slip zones to back-arc rifting systems. Furthermore, our indirect inference of fault rheology is complemented by direct imaging methods. For example, a seismic tomography study in Eastern Anatolia by Toker and Şahin (2019) used the Poisson's ratio to map crustal properties. They found that high Poisson's ratios (>0.29) correlate with ductile, melt-rich zones (analogous to velocity-strengthening areas), while low ratios (~0.23) suggest brittle, deformable crust (analogous to velocity-weakening asperities).

### 4.2. Transient shallowing of the Brittle-Ductile transition depth

To determine the temporal depth variation of aftershock sequences in this study, we calculate the different transition depth types (i.e., D85, D90, D95), defined as the depths above which conventional percentages (i.e., 85 %, 90 %, 95 %) of earthquakes occurred (Fig. 6). These cut-off depths are generally used as an indicator of the brittle-ductile transition depth (Cheng and Ben-Zion, 2019; Rolandone et al., 2004). Here, the low magnitude completeness of the relocated aftershock catalogs permits us to probe the temporal variations of transition depth in high resolution (Fig. 6). Considering that the transition depth is potentially sensitive to the choice of event windows in temporal aftershocks, we set different window sizes to check the reliability of the transition depth and to find a stable rate of depth shallowing (Fig. S6 and Table S3). The rates of transition depth shallowing for the Yangbi case (0.3–0.4 km/day), the Maduo case (0.1–0.8 km/day) and the Menyuan case (0–0.1 km/day) vary with different transition depths and window sizes (Fig. 6 and Table S3). The temporal transition depth variations of the three aftershock sequences exhibit a consistent transient shallowing, even when aftershocks from the first day are not considered (Fig. S7). In addition, a plot of depth against logarithmic time also shows the consistent sharp depth deepening during approximately the first day after the mainshock, followed by depth shallowing (Fig. S8). This indicates aftershocks experienced a process of abruptly deepening just after the mainshock and then gradually becoming shallower. Most of the transient deep early aftershocks are related to the mainshocks in space and time. Thus, these shallowing events are causally related to the mainshock ruptures and are not caused by analysis artifacts and/or location errors (Cheng and Ben-Zion, 2019).

We find that the shallowing rate of the Yangbi aftershock sequence is the most stable and least affected by both the window sizes and transition depth types, with an overall coefficient of variance < 10 % (CV, the ratio of standard deviation to mean, Table S3), while the stability of the shallowing rate in the other two cases is relatively poor with smallest CV being 18 % and 30 % for the Maduo and Menyuan cases, respectively. The most confident results for the Yangbi case can be explained by the relatively dense seismic stations and the availability of one station only 2 km from the epicentral area (Fig. 1 and Table S3). The station density and spatial distribution are relatively poor for Maduo and Menyuan cases, which is also reflected in the fact that these two cases have larger magnitudes of completeness (Fig. S1). Overall, depth shallowing rates are less affected by the transition depth type than the event window size for each case. In addition, the stricter transition depth type (i.e., D95) prefers to result in more stable shallowing rates. Therefore, the D95 type is preferred in the subsequent analysis to make a better comparison with previous studies (Cheng and Ben-Zion, 2019; Rolandone et al., 2004). We suggest that the preferred depth shallowing rates are 0.36, 0.73 and 0.09 km/day, and the corresponding window sizes are 250, 150 and 100 for the Yangbi, the Maduo and the Menyuan cases, respectively. This implies that different event window sizes are required to determine the relatively stable shallowing rate for different cases. Aside from the different magnitudes of completeness, the largest shallowing rate in the Maduo case may be explained by the relatively larger magnitude (Mw 7.4) of the mainshock that caused relatively stronger stress/strain perturbations (Cheng and Ben-Zion, 2019). The difference in mainshock magnitude cannot explain the rate discrepancy between the Yangbi and Menyuan cases. This discrepancy may be attributed to the effective viscosity of the fault materials (Ben-Zion and Lyakhovsky, 2006). The short shallowing duration after the Yangbi earthquake may be attributed to the lower effective viscosity, which is confirmed by the higher heat flow (~75 mW/m$^2$) in the Yangbi region than that (~65 mW/m$^2$) in the Menyuan region (Hu et al., 2000), and lower Vs (3.3–3.4 km/s) at 20 km depth in the Yangbi region than that (3.4–3.5 km/s) in the Menyuan region (Liu et al., 2021; Shen et al., 2016). This is similar to the shallowing duration of the 2010 Mw 7.2 El Mayor-Cucapah earthquake, which is shorter than those of the 1992 Mw 7.3 Landers and the 1997 Mw 7.3 Hector Mine earthquakes because of the lower effective viscosity, as confirmed by the higher heat flow and lower velocity observed to the south in Baja California (Cheng and Ben-Zion, 2019).

The consistent shallowing trend of the transition depth of aftershocks revealed in this study indicates that moderate-large events play a significant role in the stability of seismogenic base zone. This temporal shallowing of the brittle-ductile transition depth is also observed after the other strike-slip earthquakes (Cheng and Ben-Zion, 2019; Rolandone et al., 2004). The depth of the brittle-ductile transition is related to the rheological parameters and variations in the crust temperature and lithology (Rolandone et al., 2004). However, the temporal variations in transition depth are closely correlated with the occurrence of strong earthquakes. The depth shallowing of aftershocks over time highlights the significance of rheological control on the depth of the brittle-ductile transition and the temporal earthquake depth distribution (Rolandone et al., 2004). Thus, the pattern of transient deepening in early aftershock sequences followed by transient shallowing of the brittle-ductile transition depth during the postseismic period could be interpreted as strain-rate-dependent changes around and below the bottom of the seismogenic zone caused by ruptures of large events (Cheng and Ben-Zion, 2019; Rolandone et al., 2004). Strong earthquakes generate high stress perturbations and strain rates at the base of the seismogenic zone (Figs. 6 and 7), which control the brittle-ductile transition shallowing. Thus, the elevated stress or strain rates around the background brittle-

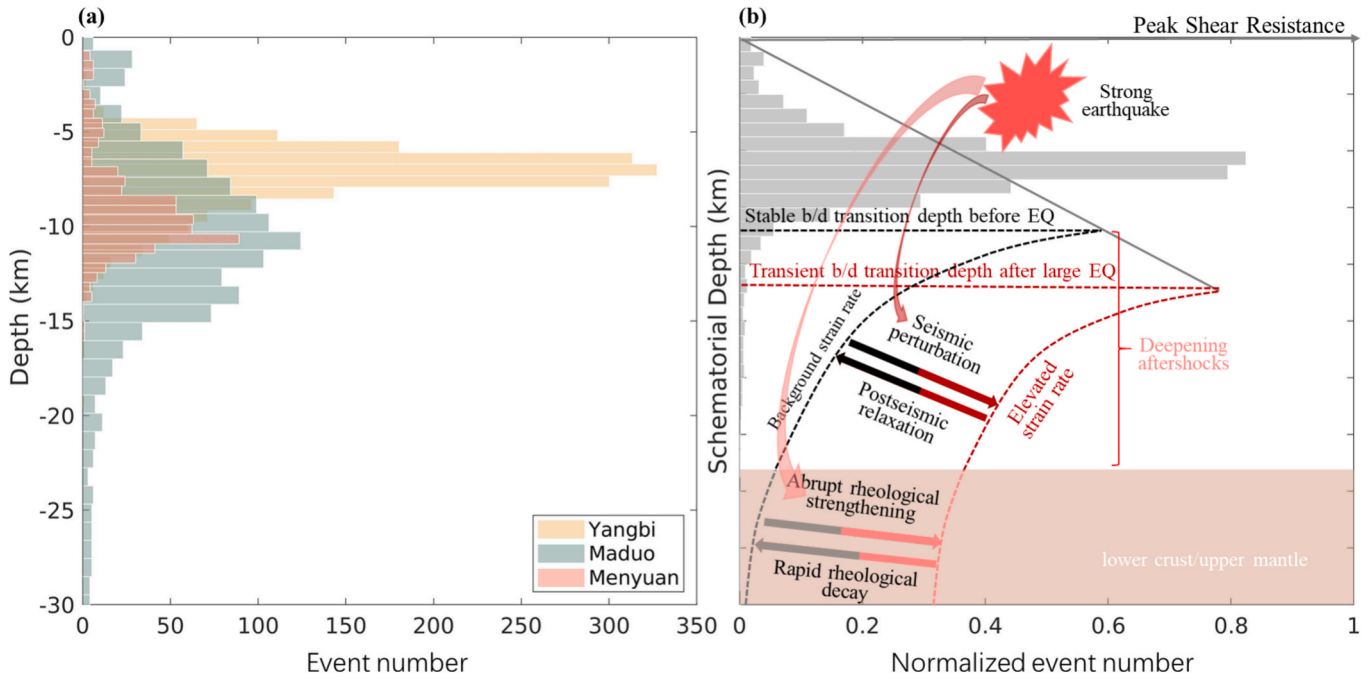


**Fig. 7.** (a) Histogram of depth distribution for the 2021 Yangbi, the 2021 Maduo and the 2022 Menyuan aftershock sequences. (b) Schematic illustration shows the mechanisms for temporally shallowing aftershocks, including the transient elevated strain rate followed by postseismic relaxations in the base of brittle-ductile (b/d in (b)) transition zone and abrupt rheological strengthening induced by strong earthquakes followed by rapid rheological decay in the lower crust and/or upper mantle.

ductile transition can produce a transition from ductile behavior (under low background strain rates, Fig. 7) to brittle response (under transient high strain rates, Fig. 7), causing abnormally deep early aftershocks (Ben-Zion and Lyakhovsky, 2006; Cheng and Ben-Zion, 2019). During the late long-term postseismic relaxation (i.e., afterslip), the transient deepening of the transition depth generally returns close to the depth of the stable brittle-ductile transition as the elevated strain rate returns to the background level, inducing the transition from brittle behavior to ductile response (Fig. 7). Unfortunately, the background brittle-ductile transition depth cannot be estimated due to the lack of high-resolution historical seismicity relocations. Considering the early afterslip dominating the early postseismic relaxation (Table S2) (Barbot et al., 2008; Liu and Xu, 2019), we suggest that the early afterslip models play a significant role in the transient depth shallowing during the early aftershock sequences. For the Menyuan earthquake, we note that while its rupture nucleated at a greater depth, the coseismic slip was predominantly shallow (Fig. 5c), with the aftershock sequence occurring mostly beneath this zone, which is in accordance with the mechanism illustrated in our schematic model (Fig. 7b).

The shallowing rates (0.1—1 km/day, Table S3) of brittle-ductile transition after the three strong strike-slip events seem to be much faster than that (~1 km/month to ~ 1 km/year) observed in previous analyses in other regions (Cheng and Ben-Zion, 2019; Rolandone et al., 2004). This rate discrepancy can be explained by the much higher afterslip moment rate at shorter duration (about one week) of our aftershock sequences than the mean value from analyses of aftershocks over several years in the Southern and Baja California (Cheng and Ben-Zion, 2019; Rolandone et al., 2004). The rapid shallowing rates are consistent with the rapid logarithmic early postseismic deformation and afterslip decay, which is generally considered one of main drivers for the aftershocks (Liu and Xu, 2019; Perfettini et al., 2018, 2019). The early GNSS postseismic deformation following the Maduo mainshock shows that the deformation during the first five days is 72 % of the total deformation of 20 days (Su et al., 2022). This indicates the relatively faster relaxation of coseismic stress disturbance in the early postseismic period, a finding that is consistent with the rapid early afterslip observed by high-rate GNSS data in other cases (Milliner et al., 2020; Tsang et al., 2019; Twardzik et al., 2019). Moreover, this is consistent with a power-law recovery of effective viscosity, that is, the effective viscosity abruptly increases during the early postseismic period (Freed and Burgmann, 2004; Qiu et al., 2018). This rapid rheological decay beneath the brittle-ductile transition depth will affect the brittle-ductile behavior in the similar way mentioned before (Fig. 7), which will play an increasingly important role as viscoelastic relaxation increasingly dominates the postseismic process over time (Diao et al., 2014; Hines and Hetland, 2016). These observations suggest that temporal shallowing of aftershocks may provide a means to probe the deep earth rheology, especially when the early postseismic geodetic data (days to weeks) are absent.

### 4.3. *Rheological and tectonic implications*

Numerical simulations predict that the aftershock migration speeds are controlled by the fault rheology (Ariyoshi et al., 2007). To resolve whether there is depth-dependent aftershock migration, the spatiotemporal evolution of aftershocks is plotted against logarithmic time at shallow and deep depths, respectively (Fig. 8). The depth-dependent aftershock migration speeds (decrease with depth) are consistently obvious in all three studied cases, which is also observed in previous studies (Frank et al., 2017; Perfettini et al., 2019). Perfettini and Ampuero (2008) propose that the transient propagation speed depends on the amplitude $\Delta\tau$ of the stress trigger (e.g., induced by coseismic ruptures) or is proportional to $\exp(\Delta\tau/A')$, where $A' = (a-b)\sigma$ is the rheological parameter with the frictional parameters $a$ and $b$. As the effective normal stress $\sigma$ is expected to increase with depth, the propagation speed should decrease with depth as observed in Fig. 8. Thus, the depth-dependent aftershock migration velocities potentially reflect the different rheological properties along the fault interface. This observation that aftershock characteristics vary with depth provides insight into crustal rheology and is not unique to our study area. A compelling parallel is the 2020 Mw 6.8 Elazığ earthquake (Irmak et al., 2021), where aftershock mechanisms were stratified by depth: shallow events

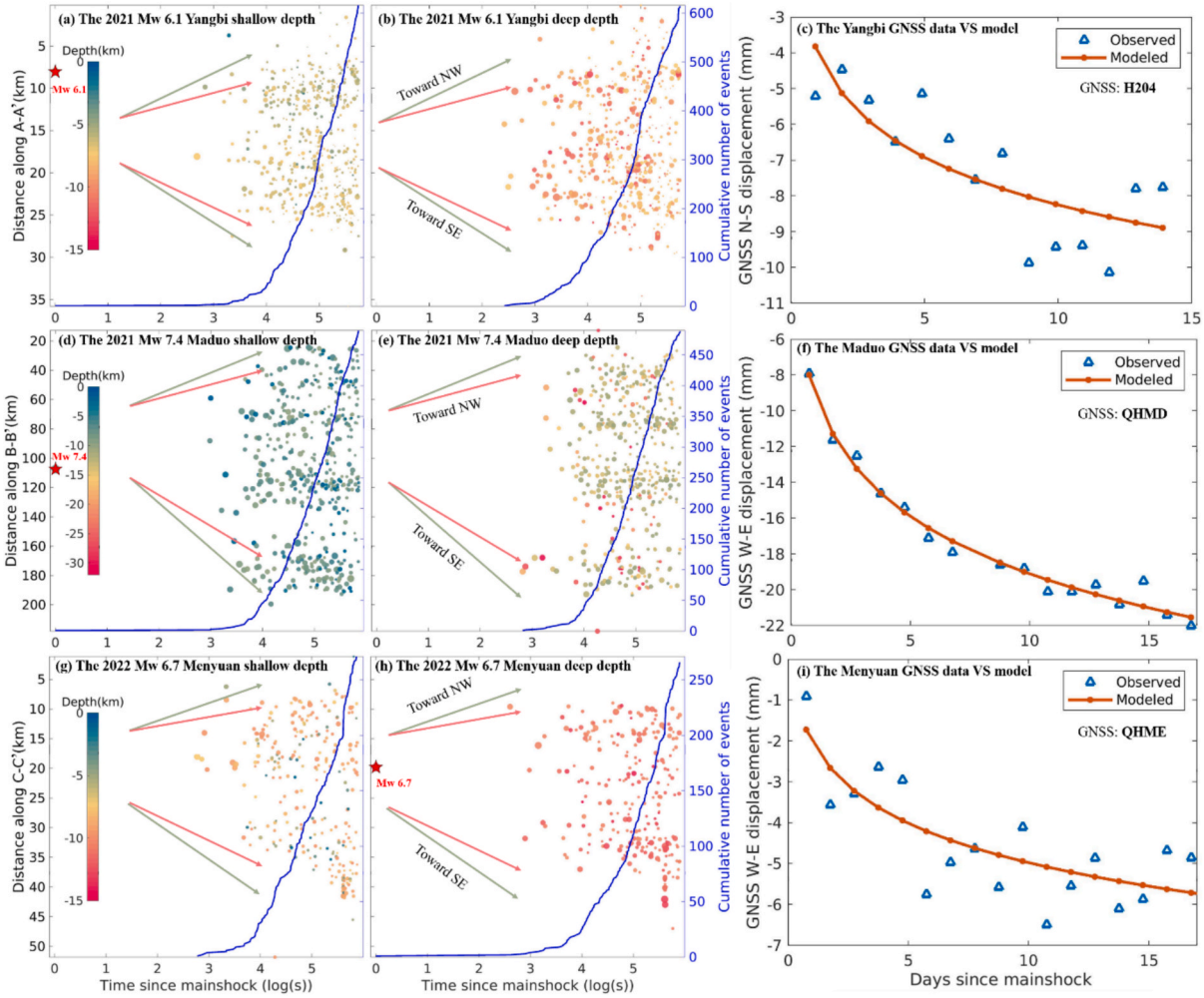


**Fig. 8.** Depth-dependent aftershock migration velocity in (left column) shallow and (middle column) deep depths, and (right column) early GNSS postseismic observations used to independently validate the aftershock-derived parameters for (a-c) the 2021 Mw 6.1 Yangbi earthquake, (d-f) the 2021 Mw7.4 Maduo earthquake and (g-i) the 2022 Mw 6.7 Menyuan earthquake. The green and red arrows show migration fronts in the shallow and deep depths, respectively. The good fit between the observed and modeled GNSS surface displacement at stations H204, QHMD and QHME (see Fig. 1) demonstrate the robustness of the aftershock-determined model parameters (see Table S4). (For interpretation of the references to color in this figure legend, the reader is referred to the web version of this article.)

showed normal faulting, while deeper events matched the mainshock's strike-slip motion, similarly reflecting a complex postseismic relaxation process.

To properly quantify these rheological parameters, we follow the assumption of aftershocks driven by afterslip within the surrounding velocity-strengthening region (Frank et al., 2017; Perfettini and Avouac, 2004):

$$N_{cum}(t) = R_L t_r log[1 + R_+/R_L(exp(t/t_r) - 1)] \quad (1)$$

where $N_{\mathrm{cum}}$ is the cumulative aftershock number, $R_L$ the long-term seismicity rate after the mainshocks are estimated based on the long-term CENC regional catalogs (Xiao and Gao, 2017; Zhang et al., 2021b), $R_{\pm}$ and $t_r$ are, respectively, the seismicity rate right after the mainshock and the duration of the postseismic deformation. It is important to note that this physics-based model is consistent with the empirical Omori's law for aftershock decay. The primary advantage of this formulation is that its parameters, particularly the characteristic duration $t_r$, can be directly linked to physical fault properties (e.g., the rheological parameter), which is a key objective of this study.

We first estimate the values of $R_{\pm}$ and $t_r$ by using nonlinear least-square fit to solve the equation (1) (Fig. 8), which reproduces well the observed cumulative seismicity numbers (Fig. S9). This velocity-strengthening model of afterslip predicts that the surface displacement $D(t)$ is proportional to the cumulative aftershock count, given by (Perfettini and Avouac, 2004):

$$D(t) = D(t=0) + \beta V_0 t_r log[1 + R_+/R_L(exp(\frac{t}{t_r}) - 1)], \quad (2)$$

where $\beta$ is a factor to scale the surface displacement and $V_0$ is the interseismic convergence rate.

Thus, the aftershock-determined model parameters can be validated by comparing the model-predicted surface displacement and the real GNSS observations. The early postseismic GNSS observations at station H204 (Zhang et al., 2021a), QHMD (Su et al., 2022) and QHME are well fit by the model-predicted surface displacements computed with equation (2), indicating the aftershocks-derived parameters are independently validated by GNSS data.

The rheological parameter $A'$ and the stressing rate $\dot{\tau}$ are related to the aftershocks-derived parameters $R_{\pm}$ and $t_r$:

$$A' = (a-b)\sigma = \Delta CFS/log(R_+/R_L), \dot{\tau} = A'/t_r, \quad (3)$$

where $\Delta CFS$ is the static Coulomb stress change induced by coseismic rupture.

To constrain rheological parameter $A'$, the $\Delta CFS$ on the seismogenic

fault interfaces was calculated using the Coulomb 3.3 software (Toda et al., 2011). These calculations utilized the coseismic slip models for the Yangbi case (Li et al., 2022), the Maduo case (Zhao et al., 2021) and the Menyuan case (He et al., 2024) as inputs (Fig. S10). The rheological parameter $A'$ and the stressing rate $\dot{\tau}$ can be computed with equation (3). The values of $A'$ and $\dot{\tau}$ in shallow depths are slightly larger but comparable to those at deep depths for each aftershock sequence (Table S4), which is consistent with the weak variation of $A'$ and $\dot{\tau}$ over the shallow 20 km depth range for the 2015 Mw 8.3 Illapel megathrust earthquake sequence (Frank et al., 2017). The values of parameter $A'$ are, respectively, about 0.1 MPa, 1 MPa and 0.45 MPa for the Yangbi case, the Maduo case and the Menyuan case. These values are comparable to the previous estimates of $A'$ [0.1 MPa − 1 MPa] derived from postseismic observations in different tectonic settings (Perfettini et al., 2010; and references therein). This confirms indirectly our interpretation of aftershocks driven by afterslip.

Assuming the $\sigma = \rho g h$, where $\rho$ is the rock density (3000 kg/m$^3$ in this study), $g$ and $h$ are, respectively, the Earth gravity constant 9.8 m/s$^2$ and fault depth, the frictional parameter $a-b$ (Table S4) in shallow and deep depths for each aftershock sequence is estimated with equation (3). The resulting values of $a-b$ (between $10^{-4}$ and $10^{-3}$) are consistent with the estimates from laboratory experiments (Marone, 1998) and the natural earthquake cases in various tectonic settings (Frank et al., 2017; Hsu et al., 2006; Liu and Xu, 2019). The evolution of $a-b$ with depth is consistent for all the three earthquake cases and show that $a-b$ decreases with depth, which are comparable to the depth-dependent $a-b$ evolutions found in the other cases (Frank et al., 2017). Coincidentally, this depth-dependent $a-b$ evolutions including its magnitude are consistent with the frictional parameter $a-b$ (between $10^{-4}$ and $10^{-3}$) estimated with the temporal afterslip derived with time-series InSAR observations following the 2021 Maduo mainshock (Zhao et al., 2022). This implies that relocated aftershock sequence could shed light on the rheological properties of deep structures, even in the absence of postseismic deformation observations.

The values of mean stressing rate $\dot{\tau}$ at shallow and deep depths are, respectively, about 0.025 MPa/year, 0.045 MPa/year and 0.05 MPa/year for the Yangbi case, the Maduo case and the Menyuan case (Table S4). With the parameter $\dot{\tau}$, an approximate recurrence time $T_{rec}$ for each case in this study can be determined using the mean coseismic stress drop $\Delta\tau$ in the main coseismic slip region (Table S4). The recurrence times are 124 years, 383 years and 207 years for the Yangbi Mw 6.1 earthquake, the Maduo Mw 7.4 earthquake and the Menyuan Mw 6.7 earthquake, respectively. The fault-parallel slip rate at the 2022 Menyuan earthquake region are well studied. The geological slip rate at Lenglongling Fault is about 4 mm/year (He et al., 2010; Zheng et al., 2013), which is well consistent with the geodetic (GPS and InSAR) slip rates between 3.9 mm/year and 4.5 mm/year (Huang et al., 2022; Li et al., 2016). Assuming that the recurrent Mw 6.7 earthquake in the region of the 2022 Menyuan earthquake causes the same surface displacement, we estimated the recurrence time (364 years) of the Menyuan Mw 6.7 earthquake by the precise mean pure strike slip in the region within about 4 km distance to the fault trace (Fig. S11 and Table S5), where coseismic surface displacement is greater than 30 % of the maximum of fault-parallel horizontal displacement induced by the 2022 Menyuan mainshock (Liu et al., 2022a), divided by the long-term interseismic slip rate of 4 mm/year (He et al., 2010; Huang et al., 2022; Li et al., 2016; Zheng et al., 2013). As the seismogenic fault hosting the 2021 Mw 7.4 Maduo earthquake is a secondary fault within the Bayan Har Block (Fig. 1), the slip rate on it is poorly studied. However, it has recently been estimated to be 1.2 mm/year by sparse GNSS observations (Zhu et al., 2021). Using the same strategy as the Menyuan case, we estimated its recurrence time of 1640 year based on the mean horizontal displacement (Fig. S12) induced by the 2021 Maduo mainshock (Liu et al., 2022b), which should be verified by subsequent paleo-earthquake studies (e.g., trench excavation across the 2021 Maduo seismogenic fault). In addition, the recurrence time estimated based on the coseismic finite fault slip model shows larger $T_{rec}$ than that estimated from fault-parallel displacement (Table S5). Overall, the displacement-derived and finite-fault-slip-derived $T_{rec}$ is much larger than our aftershocks-derived $T_{rec}$, which is expected due to the stressing rate in the early postseismic period being much larger than the long-term interseismic mean stressing rate (Frank et al., 2017). This suggests that the stressing rates during the earthquake cycle are not constant, and thus the recurrence time estimated based on early aftershocks may be the lower limit of $T_{rec}$. For the 2021 Mw 6.1 Yangbi earthquake, however, due to its small magnitude and limited rupture not breaking the surface, it is difficult to obtain a reliable recurrence time even if with the trench excavation observations. Aftershock-derived recurrence times provide an alternative approach to approximate the recurrence periods for moderate earthquakes, especially for newly discovered blind faults (that have not ruptured to the surface), such as the 2021 Yangbi seismogenic fault.

## Conclusions

We studied the early afterslip and the spatiotemporal distribution characteristics of the early postseismic sequences following the 2021 Yangbi Mw 6.1, the 2021 Maduo Mw 7.4 and the 2022 Menyuan Mw 6.7 earthquakes in eastern Tibet. Based on high aftershock migration speeds (1–100 km/day) and the dominant aseismic moment release during the early postseismic period, and a spatially complementary pattern between aftershocks, coseismic slip and afterslip, we found that the aftershocks are driven by the coseismic stress-driven early afterslip and their evolution is controlled by heterogeneous frictional properties on crustal faults. Statistical analysis shows the rapid temporal shallowing of the brittle-ductile transition depth of early aftershock sequences is mainly driven by early postseismic relaxation (i.e., afterslip). We show for the first time the variation of the aftershock-derived rheological and frictional parameters with depth for the three strike-slip faults, which is important for better understanding the evolution of eastern Tibet. The aftershock-derived recurrence times are generally shorter than the geodetic/geological estimates, suggesting that the loading rates during the earthquake cycle are not constant. We demonstrate how early aftershock sequences can provide alternative constraints to probe deep-earth rheology, especially when the early postseismic geodetic data are absent. A detailed spatiotemporal comparison between aftershocks, coseismic slip and afterslip further allows us to discriminate different aftershock driving mechanisms, whose role is important to decipher regional seismotectonics and earthquake hazards.

## CRediT authorship contribution statement

**Xiaoge Liu:** Writing – review & editing, Writing – original draft, Visualization, Validation, Software, Methodology, Investigation, Funding acquisition, Formal analysis, Data curation, Conceptualization. **Wenbin Xu:** Writing – review & editing. **William B. Frank:** Writing – review & editing, Investigation, Formal analysis. **Yijian Zhou:** Writing – review & editing, Formal analysis, Data curation. **Guoqiang Zhao:** Writing – review & editing, Data curation. **Lihua Fang:** Writing – review & editing, Formal analysis. **Hui Huang:** Writing – review & editing, Formal analysis. **Lijia He:** Writing – original draft, Formal analysis. **Weijun Gan:** Writing – review & editing, Data curation.

## Declaration of competing interest

The authors declare that they have no known competing financial interests or personal relationships that could have appeared to influence the work reported in this paper.

## Acknowledgements

We would like to extend our sincere thanks Sigurjón Jónsson, Yuan Gao, Zhuo Xiao, Xiaoning Su, Gaohua Zhu, Dezheng Zhao, Yaozong Zhou, Lei Zhao and Zilong He for their valuable suggestions, data sharing and communications during the development of this work. We acknowledge Crustal Movement Observation Network of China (CMONOC) for providing GNSS data at station QHME (https://data.earthquake.cn/datashare/report.shtml?PAGEID = siteInfo_jizhun). The GNSS postseismic data at station QHMD and H204 are available from Su et al., (2022) and Zhang et al., (2021a), respectively. The three aftershocks catalogues used in this study are respectively available from (Fan et al., 2022; Wang et al., 2021; Yang et al., 2021). The background seismicity catalogues for northeastern Tibet and southeastern Tibet is available from Xiao and Gao (2016) and Zhang et al., (2021b), respectively. Raw InSAR data are freely available (https://browser.dataspace.copernicus.eu/). This work was supported by the State Key Laboratory of Geohazard Prevention and Geoenvironment Protection Independent Research Project (SKLGP2024Z016), the National Natural Science Foundation of China (No. 42174023), Sichuan Province Science Fund (No. 2024NSFSC0802). The figures were prepared using the Generic Mapping Tools software (https://www.generic-mapping-tools.org/) and the MATLAB software (https://www.mathworks.com/products/matlab.html).

## Appendix A. Supplementary data

Supplementary data to this article can be found online at https://doi.org/10.1016/j.jag.2025.104770.

## Data availability

Data will be made available on request.

## References

Ariyoshi, K., Matsuzawa, T., Hasegawa, A., 2007. The key frictional parameters controlling spatial variations in the speed of postseismic-slip propagation on a subduction plate boundary. Earth Planet. Sci. Lett. 256, 136–146.
Barbot, S., Hamiel, Y., Fialko, Y., 2008. Space geodetic investigation of the coseismic and postseismic deformation due to the 2003 Mw7. 2 Altai earthquake: Implications for the local lithospheric rheology. J. Geophys. Res. Solid Earth 113.
Ben-Zion, Y., Lyakhovsky, V., 2006. Analysis of aftershocks in a lithospheric model with seismogenic zone governed by damage rheology. Geophys. J. Int. 165, 197–210.
Chen, X., Shearer, P.M., Abercrombie, R.E., 2012. Spatial migration of earthquakes within seismic clusters in Southern California: evidence for fluid diffusion. J. Geophys. Res. Solid Earth 117, n/a-n/a.
Cheng, Y., Ben-Zion, Y., 2019. Transient Brittle-Ductile transition Depth Induced by Moderate-Large Earthquakes in Southern and Baja California. Geophys. Res. Lett. 46, 11109–11117.
Diao, F., Xiong, X., Wang, R., Zheng, Y., Walter, T.R., Weng, H., Li, J., 2014. Overlapping post-seismic deformation processes: afterslip and viscoelastic relaxation following the 2011 Mw 9.0 Tohoku (Japan) earthquake. Geophys. J. Int. 196, 218–229.
Dublanchet, P., De Barros, L., 2021. Dual Seismic Migration Velocities in Seismic Swarms. Geophys. Res. Lett. 48.
Duverger, C., Godano, M., Bernard, P., Lyon-Caen, H., Lambotte, S., 2015. The 2003–2004 seismic swarm in the western Corinth rift: evidence for a multiscale pore pressure diffusion process along a permeable fault system. Geophys. Res. Lett. 42, 7374–7382.
Fan, L., Li, B., Liao, S., Jiang, C., Fang, L., 2022. Precise relocation of the aftershock sequences of the 2022 M6. 9 Menyuan earthquake. Earthq. Sci. 35, Q20220008.
Feng, W., He, X., Zhang, Y., Fang, L., Samsonov, S., Zhang, P., 2022. Seismic faults of the 2022 Mw6.6 Menyuan, Qinghai earthquake and its implication for the regional seismogenic structures. Chin. Sci. Bull.
Frank, W.B., Poli, P., Perfettini, H., 2017. Mapping the rheology of the Central Chile subduction zone with aftershocks. Geophys. Res. Lett. 44, 5374–5382.
Freed, A.M., Burgmann, R., 2004. Evidence of power-law flow in the Mojave desert mantle. Nature 430, 548–551.
He, L.J., Feng, G.C., Wu, X.X., Lu, H., Xu, W.B., Wang, Y.D., Liu, J.H., Hu, J., Li, Z.W., 2021. Coseismic and Early Postseismic Slip Models of the 2021 Mw 7.4 Maduo Earthquake (Western China) estimated by Space-based Geodetic Data. Geophys. Res. Lett. 48.
He, W., Yuan, D., Ge, W., Luo, H., 2010. Determination of the slip rate of the Lenglongling fault in the middle and eastern segments of the Qilian mountain active fault zone. Earthquake (In Chinese) 30, 131–137.
He, Z., Xu, W., Li, Z., Xie, L., Feng, G., Fang, N., Liu, X., Sun, K., Chen, Z., Zhu, Z., 2024. Co and postseismic fault slip models of the 2022 MW6. 7 Menyuan earthquake reveal conjugated faulting tectonics at the central section of the Lenglongling fault. Earthq. Sci. 37, 277–303.
Hines, T.T., Hetland, E.A., 2016. Rheologic constraints on the upper mantle from 5 years of postseismic deformation following the El Mayor-Cucapah earthquake. J. Geophys. Res. Solid Earth 121, 6809–6827.
Hsu, Y.J., Simons, M., Avouac, J.P., Galetzka, J., Sieh, K., Chlieh, M., Natawidjaja, D., Prawirodirdjo, L., Bock, Y., 2006. Frictional afterslip following the 2005 Nias-Simeulue earthquake, Sumatra. Science 312, 1921–1926.
Hu, S., He, L., Wang, J., 2000. Heat flow in the continental area of China: a new data set. Earth Planet. Sci. Lett. 179, 407–419.
Huang, H., Xu, W., Meng, L., Bürgmann, R., Baez, J.C., 2017. Early aftershocks and afterslip surrounding the 2015 Mw 8.4 Illapel rupture. Earth Planet. Sci. Lett. 457, 282–291.
Huang, Z., Zhou, Y., Qiao, X., Zhang, P., Cheng, X., 2022. Kinematics of the ~1000 km Haiyuan fault system in northeastern Tibet from high-resolution Sentinel-1 InSAR velocities: Fault architecture, slip rates, and partitioning. Earth and Planetary Science Letters 583.
Irmak, T.S., Toker, M., Yavuz, E., Şentürk, E., Güvenaltın, M.A., 2021. New insight into the 24 January 2020, Mw 6.8 Elazığ earthquake (Turkey): an evidence for rupture-parallel pull-apart basin activation along the East Anatolian Fault Zone constrained by Geodetic and Seismological data. Ann. Geophys. 64.
Jiang, J., Bock, Y., Klein, E., 2021. Coevolving early afterslip and aftershock signatures of a San Andreas fault rupture. Sci. Adv. 7, eabc1606.
Kato, A., Obara, K., 2014. Step-like migration of early aftershocks following the 2007 M-w 6.7 Noto-Hanto earthquake. Japan. Geophysical Research Letters 41, 3864–3869.
Lei, X., Wang, Z., Ma, S., He, C., 2021. A preliminary study on the characteristics and mechanism of the May 2021 M S 6.4 Yangbi earthquake sequence, Yunnan. China. Acta Seismologica Sinica (in Chinese) 43, 261–286.
Li, C., Shan, X., Zhang, G., Zhao, C., Gong, W., Zhang, Y., 2022. Slip Kinematics of the 2021 Yangbi Earthquake: Fore-Main-Aftershock Sequence Rupture along an unknown Secondary Fault of the Weixi–Qiaohou Fault. Seismol. Res. Lett. 93, 1400–1412.
Li, J., Chen, Y., Zhang, Z., Zhang, S., Yan, H., Chen, M., Zhan, W., Zhang, Y., Xu, W., Sun, R., 2025. Early viscoelastic relaxation and afterslip inferred from the postseismic geodetic observations following the 2021 Mw7. 4 Maduo earthquake. J. Geophys. Res. Solid Earth 130, e2024JB030466.
Li, Y., Shan, X., Qu, C., Wang, Z., 2016. Fault locking and slip rate deficit of the Haiyuan-Liupanshan fault zone in the northeastern margin of the Tibetan Plateau. J. Geodyn. 102, 47–57.
Liu, J., Hu, J., Li, Z., Ma, Z., Shi, J., Xu, W., Sun, Q., 2022a. Three-Dimensional Surface Displacements of the 8 January 2022 Mw6.7 Menyuan Earthquake, China from Sentinel-1 and ALOS-2 SAR Observations. Remote Sens. (Basel) 14.
Liu, J., Hu, J., Li, Z., Ma, Z., Wu, L., Jiang, W., Feng, G., Zhu, J., 2022b. Complete three-dimensional coseismic displacements due to the 2021 Maduo earthquake in Qinghai Province, China from Sentinel-1 and ALOS-2 SAR images. Sci. China Earth Sci. 65, 687–697.
Liu, X., Xu, W., 2019. Logarithmic Model Joint Inversion Method for Coseismic and Postseismic Slip: Application to the 2017 Mw 7.3 Sarpol Zahāb Earthquake. Iran. Journal of Geophysical Research: Solid Earth 124, 12034–12052.
Liu, X., Xu, W., He, Z., Fang, L., Chen, Z., 2022c. Aseismic Slip and Cascade triggering Process of Foreshocks Leading to the 2021 Mw 6.1 Yangbi Earthquake. Seismol. Res. Lett. 93, 1413–1428.
Liu, Y., Yao, H.J., Zhang, H.J., Fang, H.J., 2021. The Community Velocity Model vol 1.0 of Southwest China, Constructed from Joint Body- and Surface-Wave Travel-Time Tomography. Seismol. Res. Lett. 92, 2972–2987.
Marone, C., 1998. Laboratory-derived friction laws and their application to seismic faulting. Annu. Rev. Earth Planet. Sci. 26, 643–696.
Milliner, C., Bürgmann, R., Inbal, A., Wang, T., Liang, C., 2020. Resolving the Kinematics and Moment Release of Early Afterslip within the first Hours following the 2016 Mw 7.1 Kumamoto Earthquake: Implications for the Shallow Slip Deficit and Frictional Behavior of Aseismic Creep. J. Geophys. Res. Solid Earth 125.
Peng, Z., Zhao, P., 2009. Migration of early aftershocks following the 2004 Parkfield earthquake. Nat. Geosci. 2, 877–881.
Perfettini, H., Ampuero, J.P., 2008. Dynamics of a velocity strengthening fault region: Implications for slow earthquakes and postseismic slip. J. Geophys. Res. Solid Earth 113.
Perfettini, H., Avouac, J.P., 2004. Postseismic relaxation driven by brittle creep: a possible mechanism to reconcile geodetic measurements and the decay rate of aftershocks, application to the Chi-Chi earthquake. Taiwan. Journal of Geophysical Research: Solid Earth 109.
Perfettini, H., Avouac, J.P., 2014. The seismic cycle in the area of the 2011Mw9.0 Tohoku-Oki earthquake. J. Geophys. Res. Solid Earth 119, 4469–4515.
Perfettini, H., Avouac, J.P., Tavera, H., Kositsky, A., Nocquet, J.M., Bondoux, F., Chlieh, M., Sladen, A., Audin, L., Farber, D.L., Soler, P., 2010. Seismic and aseismic slip on the central Peru megathrust. Nature 465, 78–81.
Perfettini, H., Frank, W.B., Marsan, D., Bouchon, M., 2018. A Model of Aftershock Migration Driven by Afterslip. Geophys. Res. Lett. 45, 2283–2293.
Perfettini, H., Frank, W.B., Marsan, D., Bouchon, M., 2019. Updip and Along-Strike Aftershock Migration Model Driven by Afterslip: Application to the 2011 Tohoku-Oki Aftershock Sequence. J. Geophys. Res. Solid Earth 124, 2653–2669.
Qiu, Q., Moore, J.D.P., Barbot, S., Feng, L., Hill, E.M., 2018. Transient rheology of the Sumatran mantle wedge revealed by a decade of great earthquakes. Nat. Commun. 9, 995.

Roland, E., McGuire, J.J., 2009. Earthquake swarms on transform faults. Geophys. J. Int. 178, 1677–1690.
Rolandone, F., Bürgmann, R., Nadeau, R.M., 2004. The evolution of the seismic-aseismic transition during the earthquake cycle: Constraints from the time-dependent depth distribution of aftershocks. Geophysical Research Letters 31.
Shapiro, S.A., Huenges, E., Borm, G., 1997. Estimating the crust permeability from fluid-injection-induced seismic emission at the KTB site. Geophys. J. Int. 131, F15–F18.
Shen, W., Ritzwoller, M.H., Kang, D., Kim, Y., Lin, F.-C., Ning, J., Wang, W., Zheng, Y., Zhou, L., 2016. A seismic reference model for the crust and uppermost mantle beneath China from surface wave dispersion. Geophys. J. Int. 206, 954–979.
Soto, H., Sippl, C., Schurr, B., Kummerow, J., Asch, G., Tilmann, F., Comte, D., Ruiz, S., Oncken, O., 2019. Probing the Northern Chile Megathrust with Seismicity: the 2014 M8.1 Iquique Earthquake Sequence. J. Geophys. Res. Solid Earth 124, 12935–12954.
Su, X., Xiong, R., Meng, G., Guo, N., Yang, W., Li, Y., Wu, W., Zhao, G., 2022. The characteristics of crustal deformation and regional seismogenic environment associated with the 2021 Madoi, Qinghai M W 7.3 earthquake. Chin. J. Geophys. 65, 1032–1043.
Toda, S., Stein, R.S., Sevilgen, V., Lin, J., 2011. Coulomb 3.3 Graphic-rich deformation and stress-change software for earthquake, tectonic, and volcano research and teaching—user guide. U.S. Geol. Surv. Open File Rep. 1060, 63.
Toker, M., 2021. Symptomatic discretization of small earthquake clusters reveals seismic coupling to 2017 Bodrum earthquake (Mw 6.6) in the Gulf of Gökova (SW corner of Turkey): Viscous-compliant seismogenesis over back-arc setting. J. Afr. Earth Sc. 177.
Toker, M., Pınar, A., Hoşkan, N., 2021. An integrated critical approach to off-fault strike-slip motion triggered by the 2011 Van mainshock (Mw 7.1), Eastern Anatolia (Turkey): New stress field constraints on subcrustal deformation. J. Geodyn. 147.
Toker, M., Şahin, Ş., 2019. Crustal Poisson's ratio tomography and velocity modeling across tectono-magmatic lake regions of Eastern Anatolia (Turkey): New geophysical constraints for crustal tectonics. J. Geodyn. 131.
Tsang, L.L.H., Vergnolle, M., Twardzik, C., Sladen, A., Nocquet, J.-M., Rolandone, F., Agurto-Detzel, H., Cavalié, O., Jarrin, P., Mothes, P., 2019. Imaging rapid early afterslip of the 2016 Pedernales earthquake, Ecuador. Earth and Planetary Science Letters 524.
Twardzik, C., Vergnolle, M., Sladen, A., Avallone, A., 2019. Unravelling the contribution of early postseismic deformation using sub-daily GNSS positioning. Sci. Rep. 9, 1775.
Waldhauser, F., Ellsworth, W.L., 2000. A double-difference earthquake location algorithm: Method and application to the northern Hayward fault, California. Bull. Seismol. Soc. Am. 90, 1353–1368.
Wang, K., Peng, Z., Liang, S., Luo, J., Zhang, K., He, C., 2024. Migrating foreshocks driven by a slow slip event before the 2021 Mw 6.1 Yangbi, China earthquake. J. Geophys. Res. Solid Earth 129, e2023JB027209.
Wang, W., Fang, L., Wu, J., Tu, H., Chen, L., Lai, G., Zhang, L., 2021. Aftershock sequence relocation of the 2021 MS7.4 Maduo Earthquake, Qinghai. China. Science China Earth Sciences 64, 1371–1380.
Wen, Y., Cai, J., He, K., Xu, C., 2024. Dynamic rupture of the 2021 MW 7.4 Maduo earthquake: an intra-block event controlled by fault geometry. J. Geophys. Res. Solid Earth 129, e2023JB027247.
Wiemer, S., 2001. A software package to analyze seismicity: ZMAP. Seismol. Res. Lett. 72, 373–382.
Xiao, Z., Gao, Y., 2017. Crustal velocity structure beneath the northeastern Tibetan plateau and adjacent regions derived from double difference tomography. Chinese Journal of Geophysics (In Chinese) 60, 2213–2225.
Xu, W., Jónsson, S., Ruch, J., Aoki, Y., 2016. The 2015 Wolf volcano (Galápagos) eruption studied using Sentinel-1 and ALOS-2 data. Geophys. Res. Lett. 43, 9573–9580.
Yang, H., Wang, D., Guo, R., Xie, M., Zang, Y., Wang, Y., Yao, Q., Cheng, C., An, Y., Zhang, Y., 2022. Rapid report of the 8 January 2022 MS 6.9 Menyuan earthquake, Qinghai. China. Earthquake Research Advances 2.
Yang, T., Li, B., Fang, L., Su, Y., Zhong, Y., Yang, J., Qin, M., Xu, Y., 2021. Relocation of the foreshocks and aftershocks of the 2021 Ms6. 4 Yangbi earthquake sequence, Yunnan, China. Journal of Earth Science, 0-0.
Yoshida, K., Taira, T.a., Matsumoto, Y., Saito, T., Emoto, K., Matsuzawa, T., 2020. Stress Release Process Along an Intraplate Fault Analogous to the Plate Boundary: A Case Study of the 2017 M 5.2 Akita-Daisen Earthquake, NE Japan. Journal of Geophysical Research: Solid Earth 125.
Yu, C., Li, Z., Song, C., Han, B., Chen, B., Li, X., Peng, J., 2024. Fault structure and slip mechanics of the 2022 Mw 6.7 Menyuan earthquake revealed by coseismic rupture observations. Tectonophysics 872, 230192.
Zhang, K.L., Gan, W.J., Liang, S.M., Xiao, G.R., Dai, C.L., Wang, Y.B., Li, Z.J., Zhang, L., Ma, G.Q., 2021a. Coseismic displacement and slip distribution of the 2021 May 21, M(s)6.4, Yangbi Earthquake derived from GNSS observations. Chinese Journal of Geophysics-Chinese Edition 64, 2253–2266.
Zhang, Y., An, Y., Long, F., Zhu, G., Qin, M., Zhong, Y., Xu, Q., Yang, H., 2021b. Short-Term Foreshock and Aftershock patterns of the 2021 Ms 6.4 Yangbi Earthquake Sequence. Seismol. Res. Lett. 93, 21–32.
Zhao, D.Z., Qu, C.Y., Chen, H., Shan, X.J., Song, X.G., Gong, W.Y., 2021. Tectonic and Geometric Control on Fault Kinematics of the 2021 Mw7.3 Maduo (China) Earthquake Inferred from Interseismic, Coseismic, and Postseismic InSAR Observations. Geophys. Res. Lett. 48.
Zhao, L., Xie, L., Xu, W., Fang, N., Liu, J., Feng, G., 2022. Coseismic and early postseismic fault slip model and the seismogenic fault friction properties of the 2021 Maduo Mw7.3 earthquake. Chinese Journal of Geophysics (In Chinese with English Abstract).
Zheng, W.-J., Zhang, P.-Z., He, W.-G., Yuan, D.-Y., Shao, Y.-X., Zheng, D.-W., Ge, W.-P., Min, W., 2013. Transformation of displacement between strike-slip and crustal shortening in the northern margin of the Tibetan Plateau: evidence from decadal GPS measurements and late Quaternary slip rates on faults. Tectonophysics 584, 267–280.
Zhu, G., Yang, H., Tan, Y.J., Jin, M., Li, X., Yang, W., 2022. The cascading foreshock sequence of the Ms 6.4 Yangbi Earthquake in Yunnan, China. Earth and Planetary Science Letters 591.
Zhu, Y., Diao, F., Fu, Y., Liu, C., Xiong, X., 2021. Slip rate of the seismogenic fault of the 2021 Maduo earthquake in western China inferred from GPS observations. Sci. China Earth Sci. 64, 1363–1370.